

A New Recycled Al-Si-Mg Alloy for Sustainable Structural Die Casting Applications

Emre Cinkilic^{1,2}, Michael Moodispaw¹, Jianyue Zhang¹, Jiashi Miao¹, Alan A. Luo^{1,3*}

1. Department of Materials Science and Engineering, The Ohio State University, Columbus, OH 43210, USA
2. Now at Department of Materials Science and Engineering, Hakkari University, Hakkari 30000, Turkey
3. Department of Integrated Systems Engineering, The Ohio State University, Columbus, OH 43210, USA

*Corresponding author: Department of Materials Science and Engineering, The Ohio State University, Columbus, OH 43210, USA. E-mail address: luo.445@osu.edu(A.A. Luo).

Abstract:

The use of secondary aluminum for structural components in the automotive industry is limited by the high Fe contents in recycled alloys which often result in the formation of brittle β -Al₅FeSi phase which reduces the ductility of aluminum castings. In this study, a new secondary Al-Si-Mg alloy with high Fe content (about 0.44 wt.%) was developed for die casting applications. Based on thermodynamic modeling, manganese was added to obtain a designed Fe-to-Mn ratio of 2 which successfully suppressed the formation of β -Al₅FeSi phase, by forming α -Al₁₅(Fe,Mn)₃Si₂ phase with rounded or hexagonal morphology. Additionally, a fine needle-like π -Al₈FeMg₃Si₂ phase was also formed within the eutectic regions. The new recycled alloy showed comparable mechanical properties in as-cast and heat treated (T5 and T6) conditions to three major primary die cast alloys (≤ 0.2 wt.% Fe) with similar composition. Ductility up to 7.4% from tensile elongation was achieved in as-cast recycled alloy due to the modification and refinement of α -Al₁₅(Fe,Mn)₃Si₂ by Mn and Sr additions. Tensile elongation was further improved to 9.1% after T6 treatment as a result of dissolution of π -Al₈FeMg₃Si₂ phase, defragmentation of α -Al₁₅(Fe,Mn)₃Si₂ and the spheroidization of Si phase. This new alloy provides a promising path for increasing usage of recycled aluminum with high Fe content in structural die castings for automotive and other applications.

Keywords: Recycled aluminum, alloy development, Al-Si-Mg alloys, structural castings, Al-Fe intermetallics, solidification

33 I. Introduction

34 Lightweighting vehicles by replacing steel and iron components with aluminum castings can
35 significantly increase fuel efficiency and reduce greenhouse gas emissions during their lifetime.
36 Al-Si-Mg based alloys offer good castability, high specific strength and excellent corrosion
37 resistance, which are suitable for thin-wall automotive structural castings produced by high
38 pressure die casting process (HPDC)^[1,2]. HPDC is an efficient manufacturing technology used for
39 high volume production of automotive structural parts. In the last two decades, applications of
40 aluminum structural die castings in the automotive industry have significantly increased, replacing
41 stamped and welded steel sheet parts, such as shock towers, A or B pillars, subframes and door
42 panels. One recent development is the large single-piece body casting for Tesla Model Y, which
43 replaced 70 parts of stampings, extrusions, and castings. Aluminum castings used for structural
44 applications are currently produced using primary aluminum alloys with low impurity levels to
45 avoid the formation of detrimental intermetallic phases. Three major structural alloys used in the
46 die casting industry, i.e., Silafont-36^[3] from Rheinfelden Alloys, Aural-2^[3] from Rio Tinto and
47 EZCast^[3] from Alcoa (see **Table 1** for detailed compositions), are all produced from primary
48 aluminum. The Fe content in these alloys is kept less than 0.2 wt.%, and other impurities, such as
49 Zn and Cu, are kept less than 0.05 wt. % to ensure a ductility (tensile elongation) of at least 5%
50 for as-cast and heat-treated alloys.

51 However, the electrolysis process used in primary aluminum production is energy-intensive and
52 with considerable CO₂ emissions, which compromises the environmental benefits of
53 lightweighting vehicles via using aluminum components. On the other hand, recycling of
54 aluminum is significantly more economical, and requires only a small fraction (~5%) of the energy
55 required for primary production^[4-8]. The main limitation of recycled Al-Si-Mg alloys is that the
56 mechanical properties of these alloys, specifically ductility, can be inferior to their primary
57 counterparts, because of the accumulation of unwanted Fe through cascading recycling of unsorted
58 aluminum scrap^[5,9-13]. Iron can form several intermetallic phases, such as, θ -Al₁₃Fe₄, α -Al₈Fe₂Si,
59 β -Al₅FeSi, δ -Al₄FeSi₂, π -Al₈FeMg₃Si₂, etc., with Al, Mg and Si^[14-16]. These intermetallics
60 generally have adverse effect on the ductility and toughness of secondary Al-Si-Mg alloys, and
61 thus restrict the use of recycled alloys for structural components and other safety-critical
62 applications in the transportation industry. In addition, these structural components need to be

63 assembled with other cast, extruded, or sheet members by riveting/welding processes, which also
64 has certain ductility and/or weldability requirements.

65 The effect of Fe-containing intermetallic phases on the mechanical properties of aluminum
66 castings depends on their size, morphology, and volume fraction. Among the reported intermetallic
67 phases, β -Al₅FeSi is the most detrimental as it forms as interconnected thin-platelets during
68 solidification^[17,18]. The β -Al₅FeSi platelets have sharp tips and corners creating stress
69 concentrations that can promote crack formation and propagation. The formation of β -Al₅FeSi
70 platelets can be suppressed by adjusting Fe/Mn ratio, depending on the cooling rate during
71 solidification, by forming α -Al₈Fe₂Si and/or α -Al₁₅(Fe,Mn)₃Si₂ phases with a ‘Chinese-script’ or
72 globular morphology which is less detrimental to mechanical properties^[19,20]. In a recent
73 publication^[21], the authors investigated the relationship between Fe/Mn ratio and cooling rate and
74 proposed a formation map for Fe-containing intermetallic phases that can be used to control the
75 microstructure of Al-Si-Mg-Fe-Mn alloys with high Fe contents (0.5-1 wt.%). At low and
76 intermediate cooling rates (such as gravity sand or permanent mold casting), a Fe-to-Mn ratio of
77 ~1 can inhibit the formation of detrimental β -Al₅FeSi phase. At high cooling rates (above 65°C/s,
78 close to HPDC), the formation of β -Al₅FeSi phase can be suppressed with the Fe-to-Mn ratios
79 between ~1.6 and 3 for Al-Si alloys that contains up to 1% Fe^[21]. The precise control of Fe-to-Mn
80 ratio to obtain a refined microstructure, that contains relatively benign intermetallic phases at
81 minimal volume fractions while avoiding coarse sludge formation ($SF = (1 \times wt.\%Fe) +$
82 $(2 \times wt.\%Mn) + (3 \times wt.\%Cr)$)^[22], makes it possible to achieve high mechanical performance
83 in low-cost secondary alloys with high Fe contents for die casting applications.

84 Another important microstructure feature that has an impact on alloy ductility is the
85 morphology and size of the eutectic silicon particles^[23,24]. Si particles with acicular morphology
86 and coarse β -Al₅FeSi platelets can significantly reduce the elongation of recycled Al-Si-Mg alloys
87 and prevent them being used for safety-critical structural parts. In addition to modification of β -
88 Al₅FeSi phase by alloying with Mn, Sr-modification of eutectic Si can further enhance the
89 mechanical properties of recycled Al-Si-Mg alloys. It also has been reported that Fe-containing
90 intermetallics can be refined with additions of Sr^[25,26].

91 In recent studies, the effect of Fe-to-Mn ratio on the formation of Fe-containing intermetallics
92 and mechanical properties in Al-Mg-Si and Al-Si-Mg alloys with high Fe contents produced by
93 HPDC were investigated. Ji et al.^[27] compared the mechanical properties of Al-Mg-Si-Fe alloys

94 with and without Mn and observed a slight increase in yield strength and less severe reduction in
95 ductility of alloy when the alloys contained Mn. Bösch et al.^[9] investigated the microstructural and
96 mechanical property evolution in Al-Si-Mg alloys with 0.55% Fe with increasing concentration of
97 Mn. It was concluded that Fe-to-Mn ratio of ~1 was required to achieve the best mechanical
98 properties since the premature failure was avoided by eliminating β -phase and refining polyhedral
99 α -phase particles. The alloys investigated in both studies were produced from primary aluminum
100 and master alloys and not from actual aluminum scrap, and the purpose of both studies was to
101 provide a proof of concept to show that alloys with high-Fe contents can still achieve required
102 mechanical properties for structural casting applications. More recently, Lumley^[11] presented a
103 research on turning A356 scrap from recycled wheels through additions of ferro-manganese and
104 ferro-silicon to die-castable alloys. The investigated alloy compositions with ~0.4% Fe showed
105 good combination of mechanical properties that would allow these alloys to be used for automotive
106 structural applications. In addition, Lumley's investigation showed that it is possible to lower the
107 solution heat treatment temperature without loss in mechanical properties which is advantageous
108 to further reduce carbon-foot print of recycled aluminum alloys. Song et al.^[12] studied the effect
109 of Mn/Fe ratio on the Fe removal efficiency in Al-7Si-2.4Fe alloy and its mechanical properties.
110 The study showed that increasing Mn content was decreasing yield strength while fracture strength
111 and elongation were significantly improved.

112 The focus of this paper is to showcase the mechanical properties of a recycled Al-Si-Mg alloy
113 with high Fe content (0.44 wt.%) that was prepared from mixed aluminum scrap by a secondary
114 alloy producer and cast using vacuum-assisted high pressure die casting process. The composition
115 of the alloy was designed based on a previously developed Fe-rich intermetallic formation map^[12]
116 that correlates processing conditions and alloy composition. The mechanical properties of the new
117 recycled alloy were evaluated in as-cast and heat-treated (T5 and T6) conditions and compared
118 with primary alloy EZCast provided by Alcoa. The new recycled alloy showed comparable
119 mechanical properties with primary structural alloy EZCast, which provides a pathway to increase
120 the usage of secondary aluminum alloys in structural castings in automotive and other industries.

121

122 **II. Materials and Methods**

123 *A. Alloy Composition and Melting Procedures*

124 Ingots of a secondary aluminum alloy were prepared by Audubon Metals LLC (Henderson,
125 KY) using aluminum scrap. The alloy composition was designed based on the Fe-containing
126 intermetallic formation map as well as consideration of mechanical, corrosion and castability for
127 large and thin-wall automotive structural applications. As received ingots did not contain any Sr.
128 About 300 lbs. of ingots of the secondary alloy were remelted in an Thermtronix electric resistance
129 furnace. Sr was added during the remelting process, prior to die casting trial, using Al-10 wt.%Sr
130 master alloy rods. The composition of the secondary aluminum alloy was measured using
131 SPECTROMAXx optical emission spectrometer after addition of Al-Sr master alloy and at the end
132 of trial to monitor the possible fading of Sr content. The measured compositions of the new
133 recycled alloy are presented in **Table 1**, in comparison with the three major primary die cast
134 aluminum alloys.

135

136 ***Table 1.** The measured compositions (in wt.%) of the new secondary alloy in comparison with*
137 *commercial primary aluminum die cast alloys*

Alloy	Si	Mg	Fe	Mn	Cu	Zn	Sr
Beginning of trial	8.7	0.32	0.44	0.21	0.32	0.15	0.009
End of trial	8.6	0.32	0.44	0.22	0.32	0.15	0.008
<i>Silafont 36</i> ^[3]	<i>9.5-11.5</i>	<i>0.1-0.5</i>	<i><0.15</i>	<i>0.5-0.8</i>	<i><0.03</i>	<i><0.07</i>	<i>0.01-0.02</i>
<i>Aural 2</i> ^[28]	<i>9.5-11.5</i>	<i>0.27-0.33</i>	<i>0.15-0.2</i>	<i>0.45-0.55</i>	<i><0.03</i>	<i><0.03</i>	<i>0.01-0.016</i>
<i>EZCast (C448)</i> ^[28]	<i>9-11.5</i>	<i>0.15-0.8</i>	<i>0.2</i>	<i>0.1-0.8</i>	<i><0.05</i>	<i><0.05</i>	<i>0.01-0.025</i>

138

139 The temperature of the molten aluminum bath was set at 750 °C. To improve melt cleanliness
140 and remove hydrogen, degassing/fluxing operation was performed using a rotary degassing unit
141 (Pyrotek Star 2500, Aurora, OH) coupled with MIU-3400 flux injection unit (HA International,
142 Toledo, OH) to inject N₂ + Pyrotek 5051 coverflux. The flux was injected for 5 minutes at a rate
143 of 0.5 lbs/min while N₂ was injected for 10 minutes. The rotation speed and injection rate of N₂
144 gas was adjusted to achieve a uniform distribution of gas bubbles of optimal size to effectively
145 remove hydrogen from molten aluminum.

146 *B. Casting Operation*

147 A 250-ton die casting machine (Bühler H-250 SC, Uzwil, Switzerland), equipped with a
148 Fondarex vacuum unit (Highvac Economy 1C-250, Fondarex, Switzerland) located at the Center
149 for Design and Manufacturing Excellence (CDME) at The Ohio State University (OSU), was used
150 for the die casting experiments. An experimental casting design was used (**Figure 1**), which
151 includes test plates of 2, 3, and 5mm thicknesses and an ASTM standard round tensile bar with a
152 gauge diameter of 6 mm. Vacuum-assisted die casting process (with vacuum level in the die cavity
153 set at 85 mbar) was used to produce test specimens with minimal gas porosity caused by entrapped
154 air. The die was pre-heated to 205 °C, while the shot sleeve temperature was set at 350 °C. The
155 molten metal of 730 °C was transported to the shot sleeve using a robotic ladling arm (Rimrock,
156 Columbus, OH) equipped with a boron nitride coated steel ladle. The relatively high melt
157 temperature (730 °C) was used to avoid/minimize the formation of externally solidified products
158 (ESP) in the shot sleeve. The low die temperature (205 °C) was used to enhance cooling rate for
159 refined microstructure.

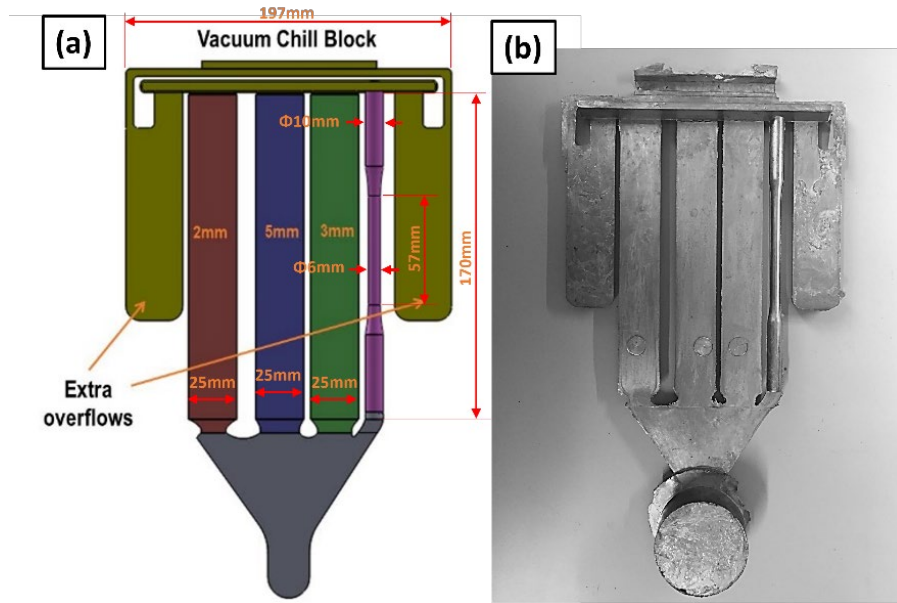
160 The shot profile was determined from the flow simulation performed using ProCast software
161 (by ESI, Farmington Hills, MI). A slow shot speed of 0.4 m/s and a fast shot speed of 1.75 m/s
162 were selected to achieve the least turbulent flow in the die cavity while achieving the required
163 vacuum level of 85 mbar. An intensification pressure of 400 bars was applied at the end of the shot
164 to minimize the level of porosity in the castings. A total of 100 shots were produced during the
165 casting trial.

166

167 *C. Heat Treatment Procedures*

168 Experimental die casting samples were quenched in water immediately after ejection. Tensile
169 bars and plates were randomly selected for further processing. Some of the samples were used for
170 mechanical testing in as-cast condition while the others were subjected to T5 and T6 heat
171 treatments, as described in **Table 2**.

172



173

174 **Figure 1** - (a) Schematic showing the experimental casting with dimensions; and (b) a die casting
 175 part produced during the casting trial.

176

177

Table 2. Summary of T5 and T6 heat treatment conditions

Temper	Solution Heat Treatment	Artificial Aging
T5	No solution heat treatment	180 °C for 2 hrs
T6	490 °C for 30 mins + quench in water at room temperature	180 °C for 2 hrs

178

179 The equilibrium isopleth calculations, where the phase constituents were mapped against
 180 temperature and Mg content (the amount of other alloying elements are fixed), in the alloy suggest
 181 that hardening phases (Al₂Cu, Mg₂Si etc.) can be decomposed at any temperature above 430 °C.
 182 Therefore, at 490 °C, Mg, Cu and Si can still be taken into solution while Si particles are
 183 spheroidized. In addition, performing the solution treatment at a lower temperature can be
 184 advantageous for reducing energy consumption and any possible distortion during quenching.

185

186 *D. Microstructure Characterization*

187 Die cast samples were sectioned and polished using standard metallographic techniques and
 188 procedures. Scanning electron microscopy (SEM) analysis was performed using an FEI Apreo

189 LoVac High Resolution electron microscope equipped with an energy dispersive spectroscopy
190 (EDS) system. Back-scatter electron (BSE) images were captured at an accelerating voltage of 10
191 kV and beam current of 1.6nA. The back-scatter detector is suitable for distinguishing Fe-
192 containing intermetallics from Si particles due to the contrast difference associated with atomic
193 number of elements.

194 Lift-out specimens for transmission electron microscopy (TEM) and scanning transmission
195 electron microscopy (STEM) characterization were prepared using an FEI Helios focused ion
196 beam system. Conventional TEM/STEM imaging and selected area electron diffraction study were
197 conducted in a FEI Tecnai F20 S/TEM microscope operating at an accelerating voltage of 200
198 keV. Atomic resolution high-angle annular dark-field (HAADF) STEM imaging was carried out
199 using a probe corrected Thermo Scientific Themis Z S/TEM microscope operated at 300 keV.

200 *E. Mechanical Property Testing*

201 The tensile properties of as-cast, T5 and T6 heat treated specimens were tested according to
202 ASTM B557 standard. Tensile testing of round bars of 6 mm diameter was conducted on an MTS
203 Criterion Electromechanical Universal Test System at room temperature, with a constant strain
204 rate of 0.005 mm/s. For each temper, at least 5 samples were tested, and the best and range of
205 properties are reported.

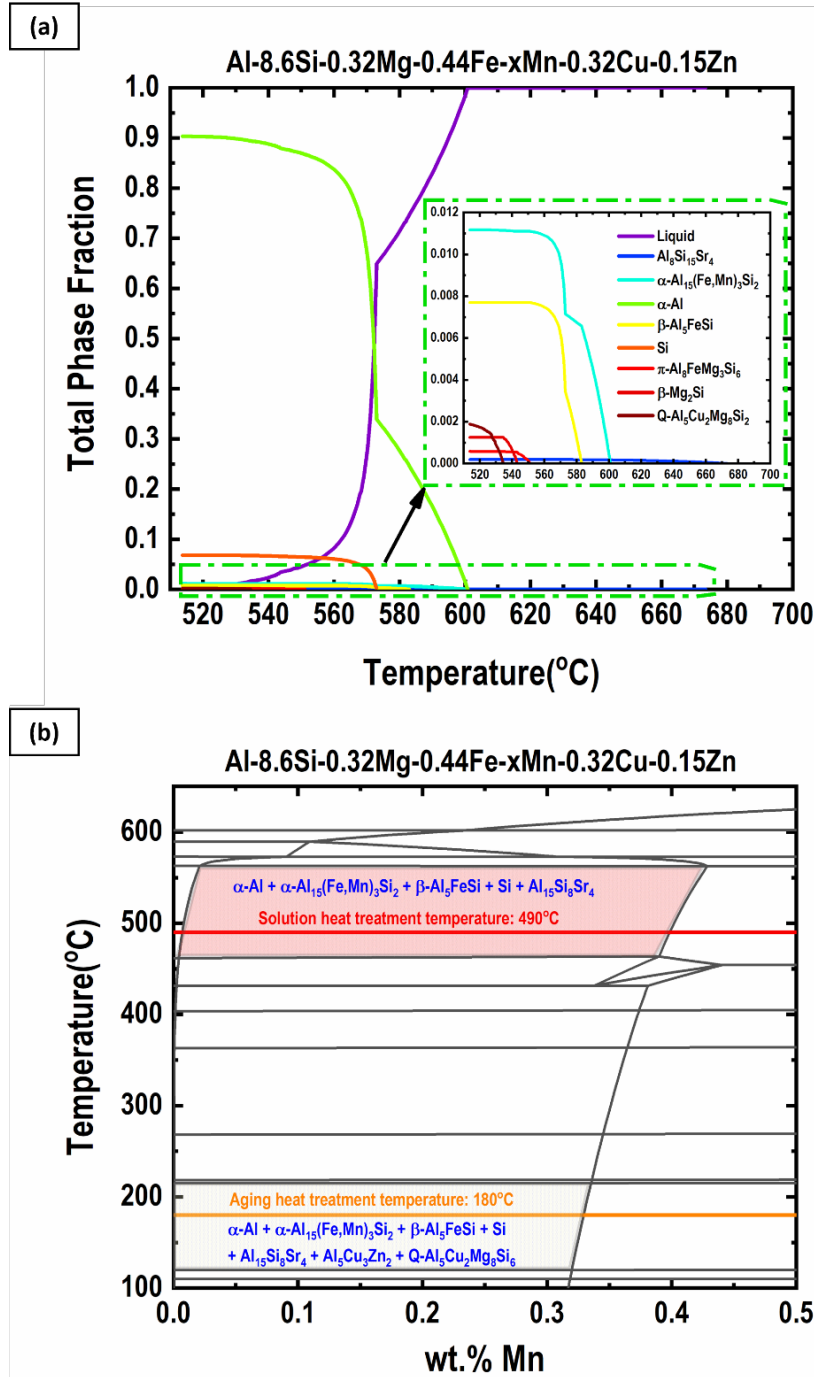
206 The bending properties of as-cast, T5 and T6 heat treated plates were measured according to
207 ASTM E290-14 Standard using the guided-bend no-die test setup. A three-point bending test was
208 used to measure the bendability of the die casting plates with different thicknesses. The specimens
209 for bending test were cut to a length of 150 mm and a width of 25 mm. The bending test was
210 conducted on an MTS Criterion Electromechanical Universal Test System at room temperature
211 with a punch radius of 12.5mm. The specimen was placed at the die and the punch speed was set
212 to 20 mm/s. The span distance (c) was set at 19 mm, 22 mm and 28 mm for 2 mm, 3 mm, and 5
213 mm thick plates, respectfully. To ensure the replicability of bending, each sample condition was
214 tested at least three times.

215

216 III. Results and Discussion

217 A. CALPHAD Modeling

218 A CALculation of PHase Diagrams (CALPHAD) analysis was performed for the secondary
219 alloy composition using Pandat software from CompuTherm LLC (Madison, WI) and PanAl2021
220 thermodynamic database to predict the microstructure and determine the heat treatment conditions
221 for the new alloy. Solidification microstructure (such as phase constituents and fractions) of
222 multicomponent alloys can be predicted using equilibrium and Scheil models. The equilibrium
223 model assumes complete mixing in both liquid and solid phases, thus, can be used to simulate the
224 as-cast microstructure of low solidification rate processes (such as sand casting) or fully annealed
225 microstructure. On the other hand, Scheil model, assuming no diffusion in solid and complete
226 mixing in liquid, provides a better approximation (than the equilibrium model) for solidification
227 microstructure for processes with high cooling rates high pressure die casting ^[29]. One exception
228 is the prediction of peritectic reactions (such as $L + \alpha\text{-Al}_8\text{Fe}_2\text{Si} \rightarrow \beta\text{-Al}_5\text{FeSi}$ in this study) where
229 solid-state diffusion, assumed to be zero in the Scheil model, is needed to facilitate the reactions.
230 Therefore, in case of recycled Al alloys with high Fe content, Scheil model cannot accurately
231 predict $\alpha \rightarrow \beta$ transformation ^[29], but still used to simulation fractions of other phases. The
232 calculated molar fractions of phases for the as-cast condition are presented in **Figure 2a**, based on
233 Scheil (non-equilibrium) model. In this new recycled alloy, the formation of $\alpha\text{-Al}_{15}(\text{Fe},\text{Mn})_3\text{Si}_2$
234 phase starts after the solidification of $\alpha\text{-Al}$ grains and continues throughout the eutectic
235 solidification. Therefore, α -phase present in the microstructure with two distinct morphologies
236 confirms the solidification sequence predicted by the Scheil simulation. Other minor intermetallic
237 phases predicted by Scheil model include $\beta\text{-Al}_5\text{FeSi}$, $\pi\text{-Al}_8\text{FeMg}_3\text{Si}_2$, Mg_2Si and $\text{Q-Al}_5\text{Cu}_2\text{Mg}_8\text{Si}_2$.
238 **Figure 2b** is a calculated equilibrium isopleth as a function of temperature and Mn content in the
239 alloy showing the domains for solutionizing and aging treatment of this new alloy.



240

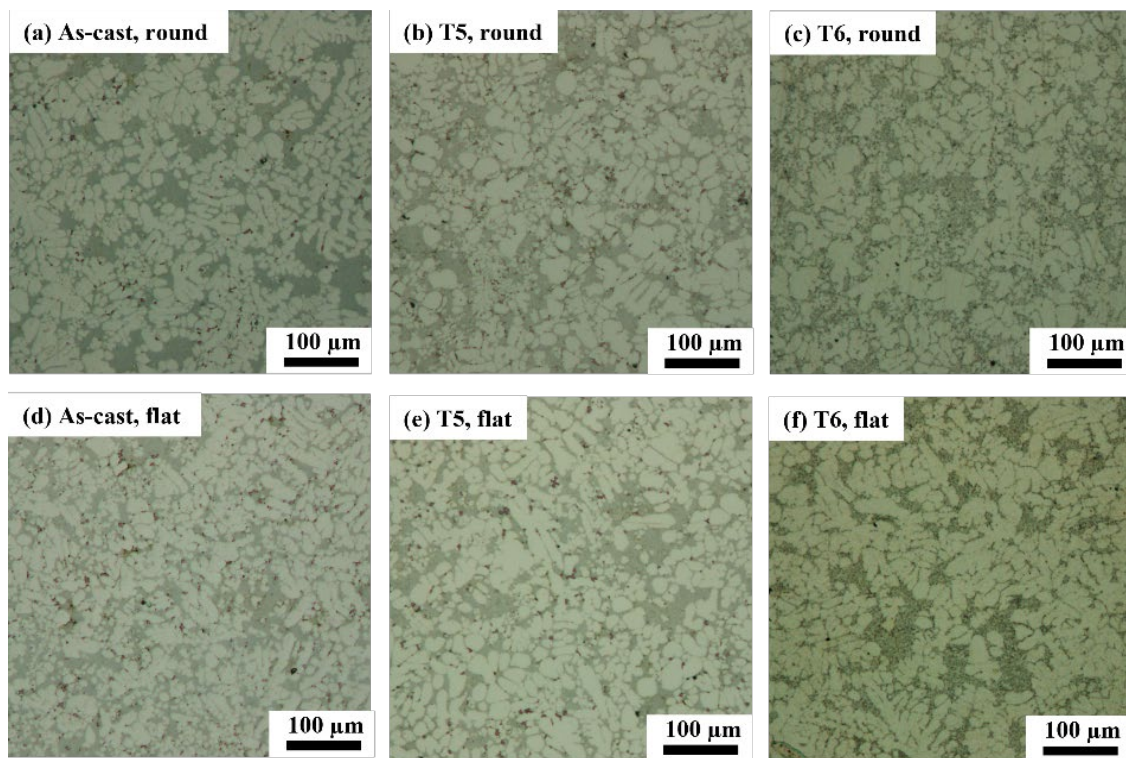
241 **Figure 2** – CALPHAD analysis performed for the composition of the secondary alloy: (a) as-cast
 242 phase fraction obtained from Scheil solidification simulation, (b) the equilibrium isopleth as a
 243 function of temperature and Mn content in the alloy showing the domains where solutionizing and
 244 aging were performed.

245

246 *B. Microstructural of Test Specimens*

247 Microstructural characterization was conducted on the cross-section of 3 mm plates and round
248 tensile bars for as-cast, T5, and T6 conditions. **Figure 3** shows optical micrographs of the recycled
249 Al alloy for different tempers of the round and flat test specimens. The as-cast microstructure
250 mainly consists of primary α -Al dendrites and the eutectic phase in both round bars and 3 mm
251 plates. There is no obvious difference in microstructural features between the round tensile bar and
252 the 3 mm plate. The cell size of α -Al dendrites ranges from 10 to 50 μ m, and the eutectic phase is
253 refined as a result of Sr-modification and rapid cooling. After the high temperature solution
254 treatment, the α -Al dendritic size does not change, indicating a good thermal stability. However,
255 the eutectic Si evolved from fine fibrous structure to spheroidized particles during the solution heat
256 treatment (**Figure 3c,f**)^[30].

257



258

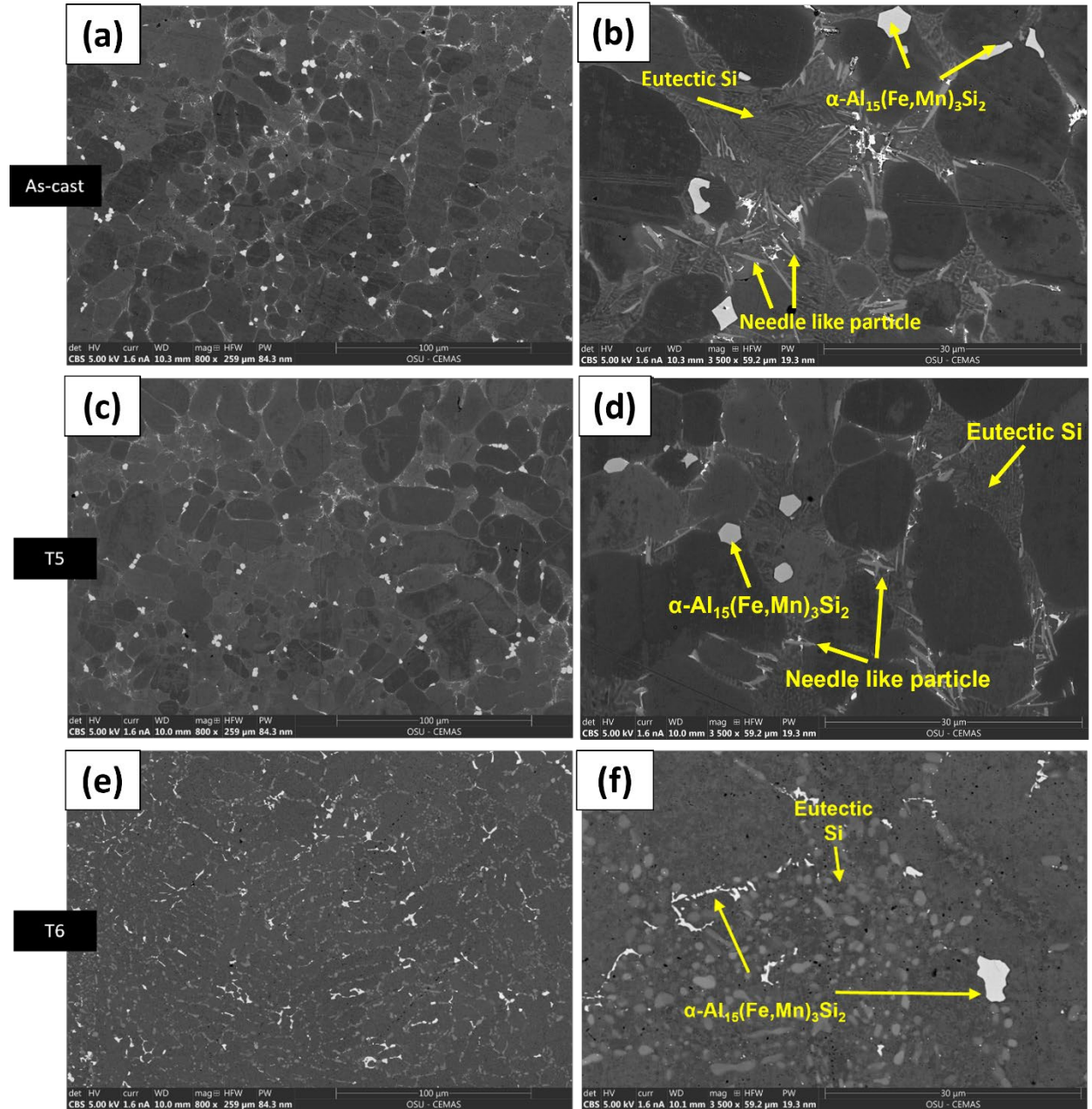
259 **Figure 3.** Optical micrographs from the round tensile bar for (a) as-cast, (b) T5, and (c) after T6;
260 and from 3 mm plate for (d) as-cast, (e) T5, and (f) T6.

261

262 To better reveal the microstructural features, the cross-sections of 3mm plate specimens in as-
263 cast, T5 and T6 treated conditions were characterized by SEM. **Figure 4** presents back-scattered
264 images of the new recycled alloy at low and high magnifications. The as-cast microstructure

265 consists of α -Al grains, α -Al₁₅(Fe,Mn)₃Si₂ phase with polygonal morphology, refined globular α -
266 Al₁₅(Fe,Mn)₃Si₂/ α -Al₈Fe₂Si phase particles, π -Al₈FeMg₃Si₂ phase with needle-like morphology,
267 and modified eutectic Si phase in the interdendritic regions. The low-magnification image (**Figure**
268 **4a**) shows an even distribution of α -Al₁₅(Fe,Mn)₃Si₂ phase with polygonal morphology between
269 the dendrites. The relatively small size and the faceted polyhedral morphology of α -
270 Al₁₅(Fe,Mn)₃Si₂ phase suggests its free growth in the interdendritic region after the formation of
271 Al grains and prior to eutectic solidification. The result indicates that the as-cast microstructure is
272 free of detrimental β -Al₅FeSi phase and confirms that combination of Fe-to-Mn ratio within the
273 range of 1.6 - 3 and rapid cooling conditions can eliminate β -phase formation. It should be pointed
274 out that the simulation results in **Figure 2a** predicted β -Al₅FeSi phase formation during Scheil
275 solidification. This discrepancy is due to an inherent problem of Scheil model being incapable of
276 simulating the peritectic reaction associated with the β -phase formation. Under rapid cooling
277 conditions as in the case of die casting process, the consecutive transformation of θ -Al₁₃Fe₄ and α -
278 Al₈Fe₂Si phase to β -Al₅FeSi can be suppressed since there is not enough time for the peritectic
279 reaction during solidification^[10,21,31].

280 The T5 (180°C for 2 hrs) microstructure, as shown in **Figure 4c,d**, is almost identical to the as-
281 cast microstructure, in terms of Fe-containing intermetallic phases that are present. The dissolution
282 of α -Al₁₅(Fe,Mn)₃Si₂ and/or π -Al₈FeMg₃Si₂ intermetallic phases at the aging temperature of 180°C
283 is thermodynamically impossible based on the CALPHAD analysis shown in **Figure 2b**. The
284 microstructure of a T6 sample (**Figure 4e,f**), which was solutionized at 490°C for 30 mins and
285 aged at 180°C for 2 hrs, shows three stark differences in comparison with both as-cast and T5
286 samples. The first is the reduced fraction of α -Al₁₅(Fe,Mn)₃Si₂ particles with polygonal
287 morphology in the T6 sample. The second is that π -phase was completely dissolved while α -
288 Al₁₅(Fe,Mn)₃Si₂ fragmented into smaller particles during the solution heat treatment procedure.
289 Finally, **Figure 4f** clearly shows eutectic Si was successfully spheroidized after a 30-minute
290 solution heat treatment.



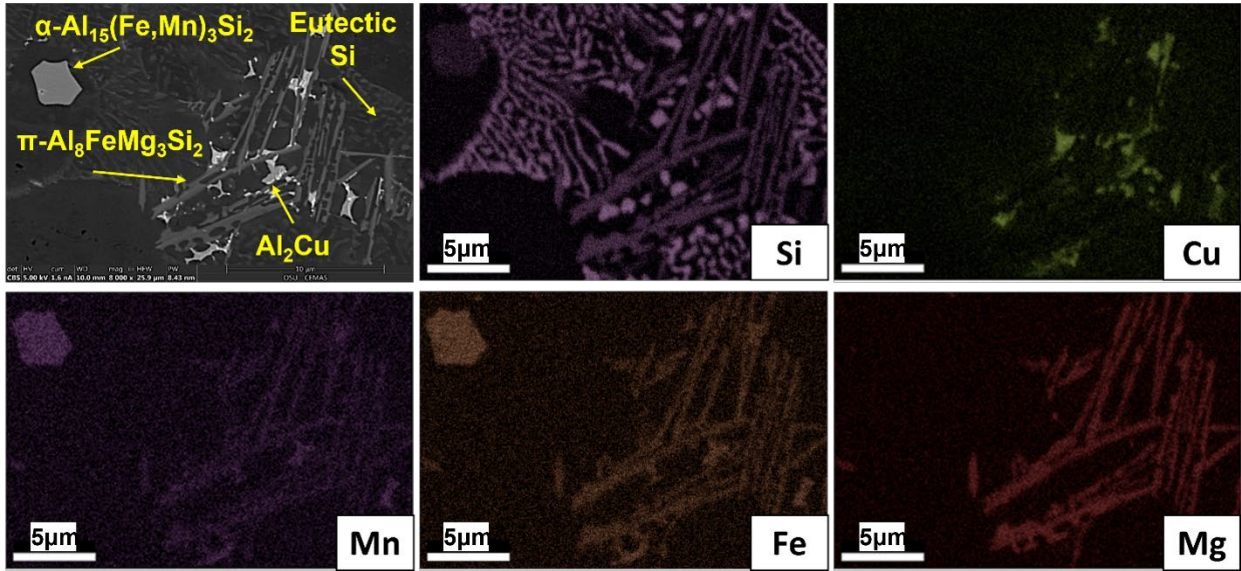
291
 292 **Figure 4** - Back-scattered SEM images obtained from cross section of 3 mm plates: (a,b) as-cast;
 293 (c,d) T5 condition; and (e,f) T6 condition.

294
 295 Since the recycled alloy contains ~ 0.3 wt.% Cu (**Table 1**), the presence of eutectic Cu-
 296 containing phases, such as $\theta\text{-Al}_2\text{Cu}$ and $\text{Q-Al}_5\text{Cu}_2\text{Mg}_8\text{Si}_2$, can be seen in the microstructure of as-
 297 cast samples (**Figure 5**). The EDS maps presented in **Figure 5** show the distribution of major
 298 alloying elements in a selected region of as-cast microstructure. The results indicate that π -phase
 299 acts as a substrate for nucleation and growth of the Cu-containing intermetallic phases. The Sr

300 addition modified the eutectic Si effectively from platelet morphology to fibrous network, which
301 is beneficial to the mechanical properties of the samples.

302 According to the equilibrium isopleth calculated in **Figure 2b**, β -Al₅FeSi phase should be
303 present in the microstructure. However, the formation of β -phase from the non-equilibrium
304 microstructure during the solutionizing was suppressed by keeping the solution heat treatment
305 duration short. α -Al₁₅(Fe,Mn)₃Si₂ phase is stable at the solution heat treatment temperature while
306 π -Al₈FeMg₃Si₂ phase cannot be present in the microstructure according to the equilibrium isopleth.
307 Since Mg and Si are relatively fast diffusing solutes in the Al matrix, the dissolution of π -phase
308 was achieved within 30 minutes and the solution heat treated microstructure was free of π -phase.
309 Although β -phase is stable at the solution heat treatment conditions, it must form through a
310 diffusion-controlled process that its rate-limited by the diffusion rate of Fe which is low in Al
311 matrix^[32].

312



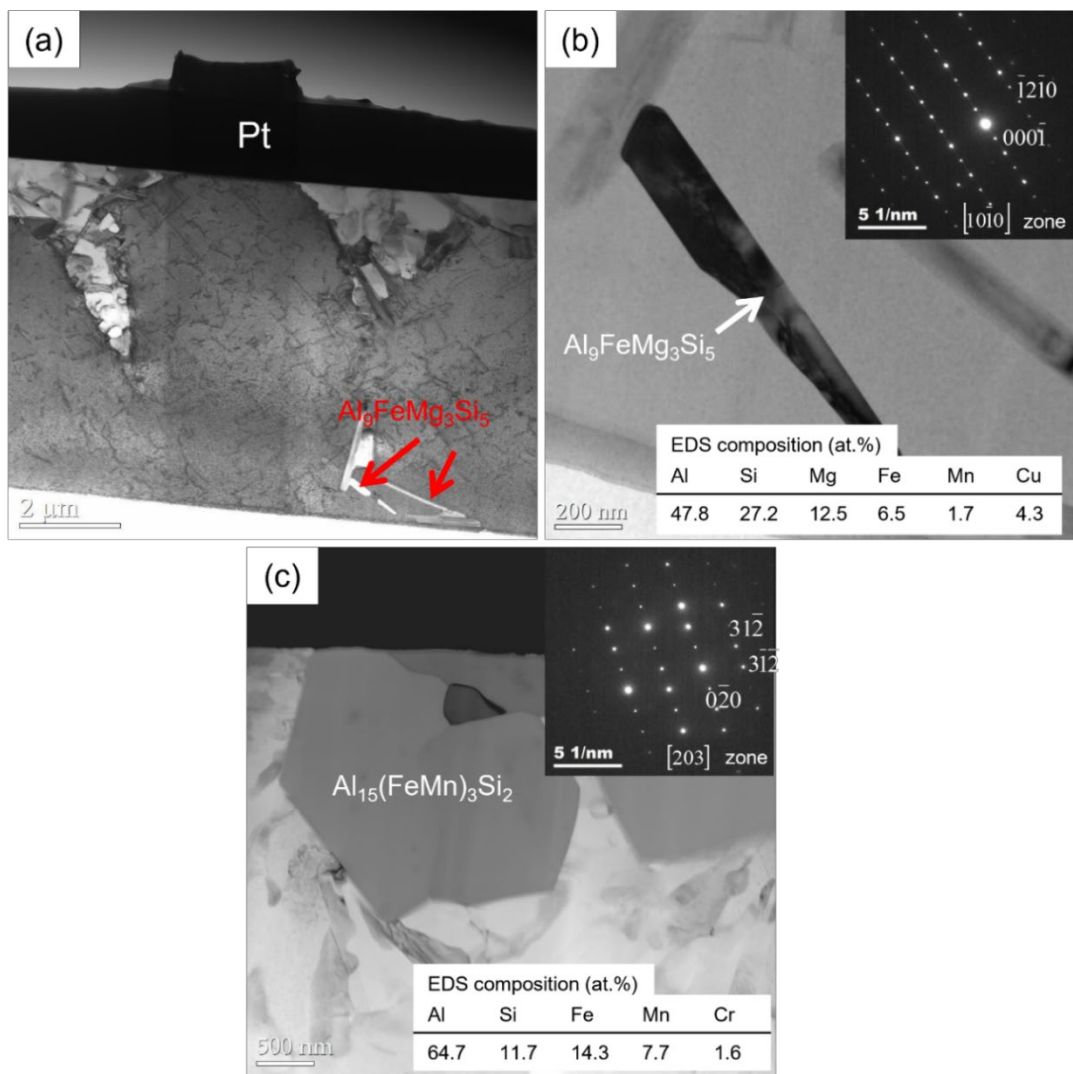
313

314 **Figure 5** - EDS maps showing the distribution of alloying elements in a selected region of as-cast
315 microstructure.

316

317 To further characterize the intermetallic phases in as-cast samples, TEM analysis was carried
318 out. **Figure 6a** is a low-magnification bright field TEM image of a fine needle-like particle. A
319 selected area diffraction pattern (SADP) confirmed that the needle-like particle is π -Al₉FeMg₃Si₅
320 and the SADP along [10 $\bar{1}$ 0] zone axis of π -phase is presented as an inset in **Figure 6b**. The
321 composition analysis on the intermetallic phase was also performed and results are also inserted

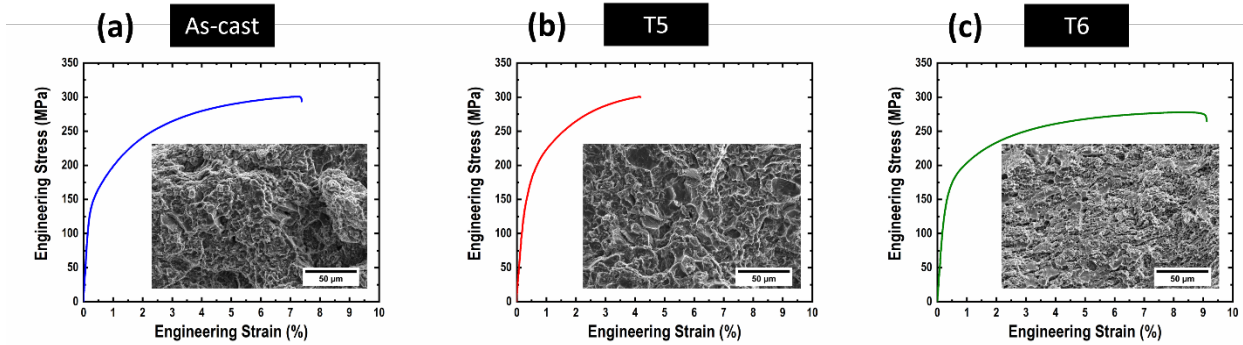
322 in **Figure 6b**. In addition to Al, Fe, Mg and Si, EDS showed that Mn and Cu are both present in
 323 π - $\text{Al}_9\text{FeMg}_3\text{Si}_5$ phase, which can dissolve some Mn since Mn can replace Fe in the crystal
 324 structure. Moreover, the presence of Cu can be explained by the bulky Al_2Cu phase nucleated on
 325 the π -phase. The particles with polyhedral morphology were also characterized by TEM (**Figure**
 326 **6c**). The EDS analysis shows it has a composition rich in Fe, Si and Mn, and the selected area
 327 diffraction pattern along its $[203]$ zone axis confirms that these bulky particles are α -
 328 $\text{Al}_{15}(\text{Fe,Mn})_3\text{Si}_2$ phase.



329
 330 *Figure 6. TEM/STEM characterization of intermetallic particles in as-cast recycled alloy, (a) a*
 331 *bright field STEM image of needle-like particle; (b) a bright field TEM image with an inset selected*
 332 *area diffraction pattern along $[10\bar{1}0]$ zone axis of π - $\text{Al}_9\text{FeMg}_3\text{Si}_5$; and (c) a bright field STEM*
 333 *image of α - $\text{Al}_{15}(\text{Fe,Mn})_3\text{Si}_2$ phase with an inset selected area diffraction pattern along its $[203]$*
 334 *zone axis. (Pt stands for platinum that was deposited on the specimen surface to protect it from*
 335 *ion damage during FIB)*

336 *C. Mechanical Properties of Secondary Alloy*

337 The mechanical properties of the new secondary alloy were evaluated through both tensile and
 338 3-point bending tests for as-cast, T5 and T6 conditions. Tensile tests were performed on round
 339 tensile bars of 6 mm in diameter. Representative stress-strain curves are presented in **Figure 7** and
 340 the tensile test results are summarized in **Table 3**. The yield strength is determined according to
 341 the 0.2% offset strain.



342

343

344 **Figure 7** - Typical tensile testing curves obtained and their respective fracture surfaces as insets:
 345 (a) as-cast; (b) T5; and (c) T6.

346

347 **Table 3.** Mechanical properties of the new recycled alloy and three major primary alloys

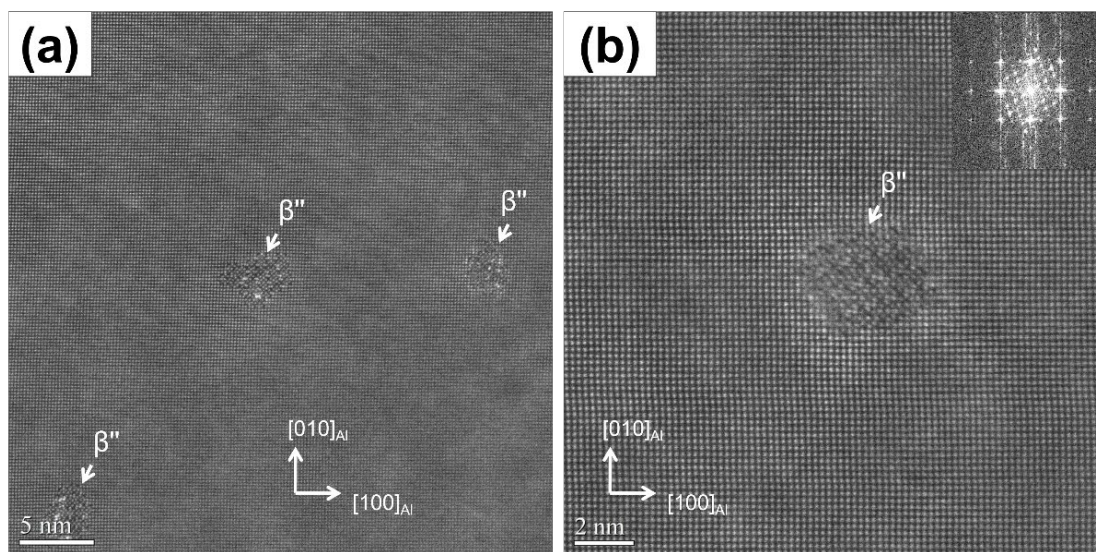
Alloy/Temper	Yield strength, MPa	UTS, MPa	Elongation, %
New Recycled Alloy/As-cast	154 ± 8	274 ± 10	5.8 ± 0.9
New Recycled Alloy/T5	194 ± 11	290 ± 16	3.7 ± 0.4
New Recycled Alloy/T6	173 ± 9	275 ± 5	7.8 ± 1.2
<i>Silafont 36/As-cast</i> ^[3]	135 (120-150)	270 (250-290)	8 (5-11)
<i>Silafont 36/T5</i> ^[3]	200 (155-245)	308 (275-340)	6.5 (4-9)
<i>Silafont 36/T6</i> ^[3]	245 (210-280)	315 (290-340)	9.5 (7-12)
<i>Aural 2/As-cast</i> ^[3]	135 (120-150)	280 (250-310)	7.5 (5-10)
<i>Aural 2/T5</i> ^[3]	170 (150-190)	285 (270-300)	7.8 (6.5-9)
<i>EZCast/As-cast</i> ^[28]	155 (148-162)	301 (287-314)	8.5 (7-10)
<i>EZCast/T5</i> ^[28]	210 (205-215)	319 (311-326)	7.25 (6-8.5)
<i>EZCast/T6</i> ^[28]	228 (221-235)	305 (299-310)	11 (8-14)

348

349 The as-cast yield strength (YS) of the new recycled alloy averaged at 154 MPa, which is similar
 350 to that of primary EZCast alloy but slightly higher YS than Silafont 36 and Aural 2, likely owing
 351 to higher Cu and Zn contents in the recycled alloy. However, ultimate tensile strength (UTS) and
 352 elongation of the secondary alloy are slightly below those of three primary alloys, which is

353 probably due to significantly higher Fe content (0.44 wt.%) in the recycled alloy. Although the
354 polygonal α -Al₁₅(Fe,Mn)₃Si₂ and needle-like π -Al₈FeMg₃Si intermetallic phases in the as-cast
355 recycled alloy are less detrimental to alloy ductility compared to β -Al₅FeSi phase, the higher total
356 fractions of Fe-containing intermetallic phases in the recycled alloy still lead to less ductility than
357 the primary alloy (0.15 wt.%).

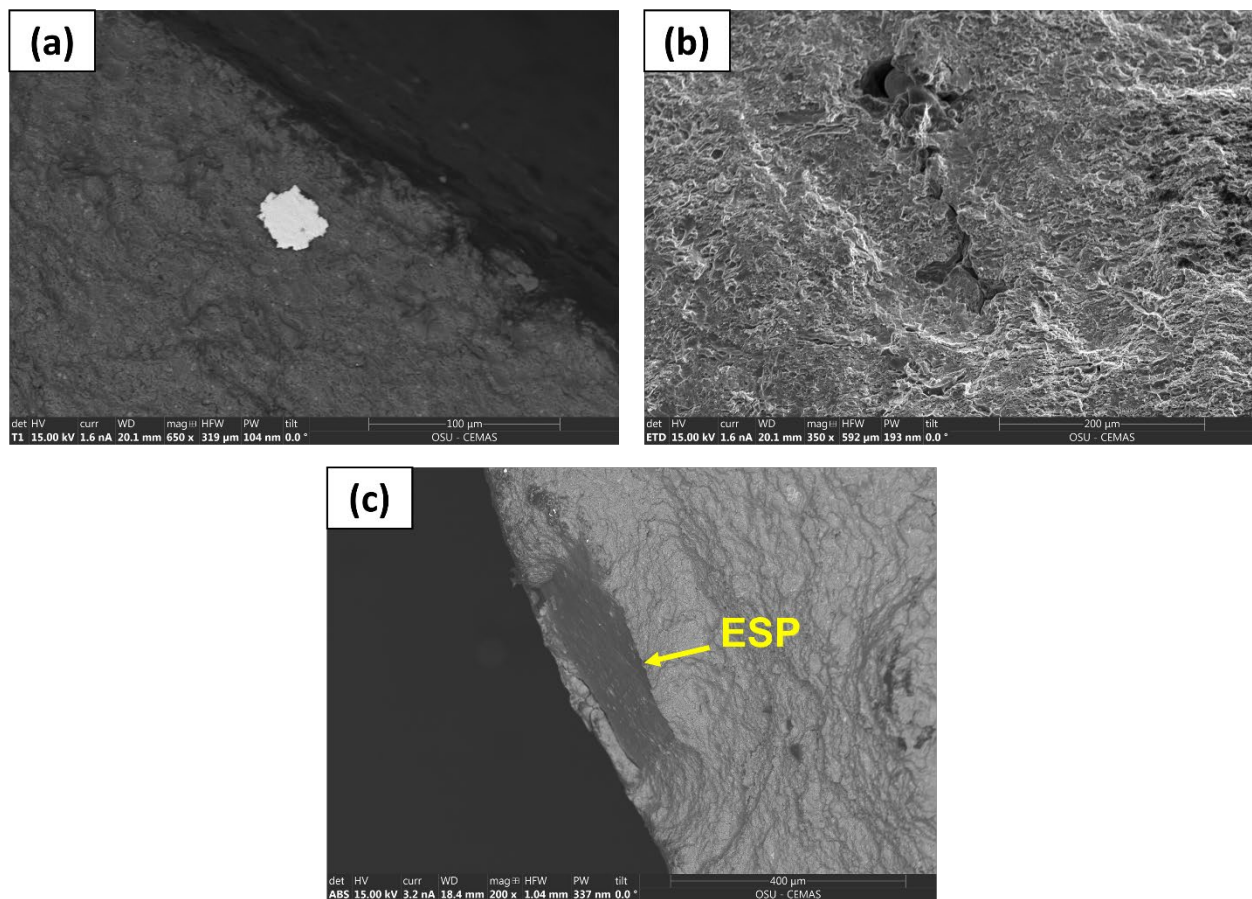
358 **Table 3** shows that a T5 treatment can increase the YS of the new recycled alloy by about 26%
359 to 194 MPa at the expense of a reduction in tensile elongation. On the other hand, T6 heat treatment
360 can improve both the YS (by about 12%) and elongation (by about 34%) over the as-cast samples.
361 To understand the strengthening mechanisms after T5 and T6 treatments, high-angle annular dark-
362 field (HAADF)-STEM images were taken to characterize the precipitation microstructure of the
363 new alloy. As shown in **Figure 8**, the precipitates with a diameter of \sim 5 nm are present in the
364 microstructure and the inset SADP indicates that they are β'' phase. This coherent β'' phase with
365 needle-shaped morphology is likely the source of strength improvements in T5 and T6 treated
366 samples. Additional microstructure changes were also noted in the T6 samples, i.e., complete
367 dissolution of needle-like π -Al₈FeMg₃Si₂ phase, the fragmentation of coarse polygonal α -
368 Al₁₅(Fe,Mn)₃Si₂ phase and spheroidization of Si particles. This explains the simultaneous increase
369 of strength and ductility from as-cast to T6 samples.



370
371 **Figure 8.** Atomic resolution HAADF-STEM images along $[001]$ zone axis of Al matrix showing
372 the β'' precipitates in T6 treated microstructure, at (a) low magnification; and (b) higher
373 magnification.

374

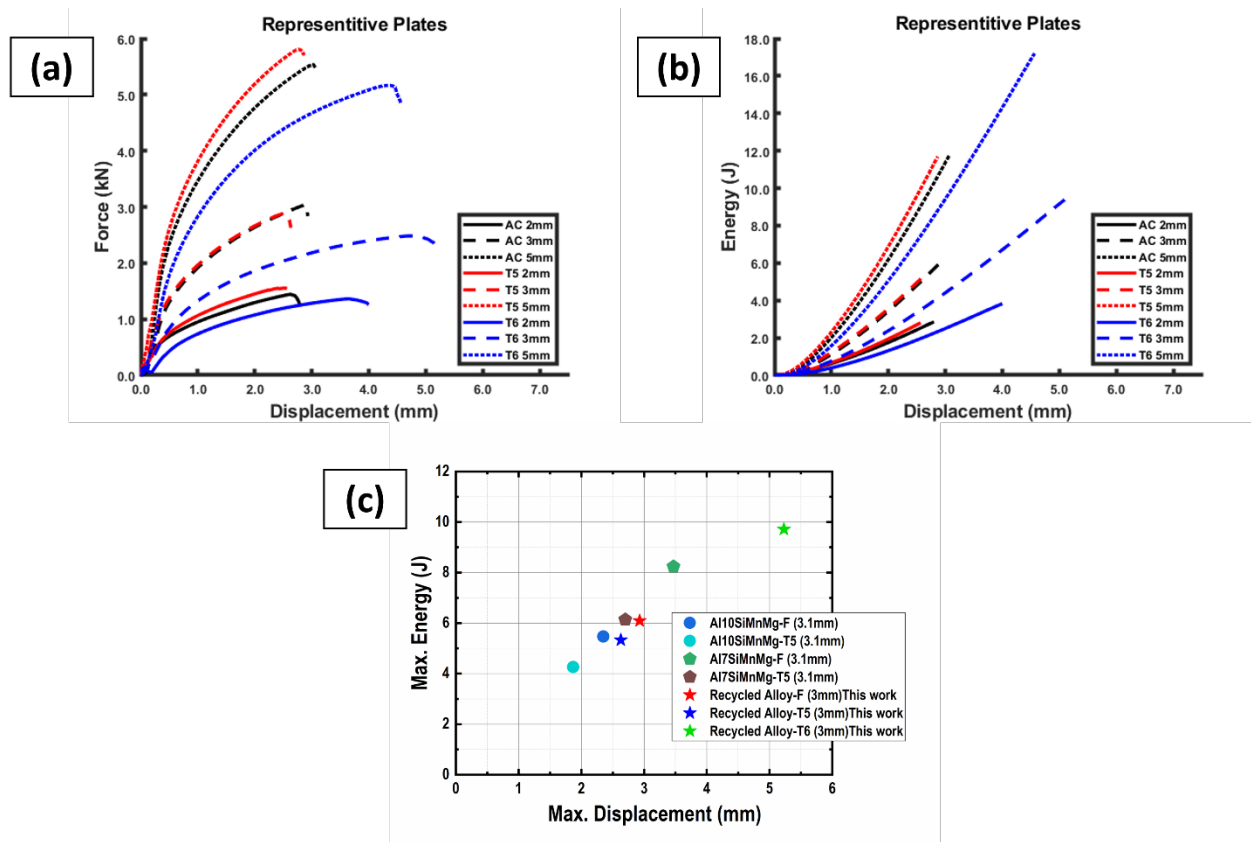
375 Even though promising elongation values of 7.4% and 9.1% were achieved for as-cast and T6
376 conditions, respectively (**Figure 7**), the new recycled alloy shows slightly lower elongation values
377 compared to the three primary alloys (**Table 3**). However, the best results of the new recycled
378 alloy are comparable with the primary alloys. Further examination of the fracture surfaces of some
379 tensile samples with low ductility, **Figure 9**, reveals porosity formation (mostly shrinkage-related),
380 entrained oxides, externally solidified products (ESP) in the die casting microstructure, which have
381 been known to adversely affect the sample ductility via promoting premature failure^[33]. It is,
382 therefore, reasonable to suggest that further optimization of die casting process parameters can
383 reduce these defects and improve ductility of the secondary alloy castings.



384
385 **Figure 9.** SEM micrographs showing (a) oxide inclusion (white); (b) shrinkage porosity; and (c)
386 externally solidified product (ESP) at fracture surfaces of as-cast recycled alloy specimens.

387
388 Another important property is bendability of an alloy which provides information on its energy
389 absorption capability, which is related to crashworthiness in automotive applications. Three-point

390 bending tests were performed to evaluate the bendability of the cast plates of various thicknesses.
 391 The sample geometry and thickness are both important factors that affect the results. As
 392 summarized in **Table 4** and **Figure 10**, the total energy absorbed by the plates increases with
 393 thickness for as-cast, T5 and T6 samples. As for the effect of heat treatment conditions, T5 treated
 394 plates of different thicknesses show lower energy absorption compared to as-cast samples. On the
 395 other hand, T6 treatment can almost double the energy absorption capability for all thicknesses.
 396 The energy absorption results for 3 mm plates were compared to results for primary Al-10Si and
 397 Al-7Si based die cast alloys with similar thickness (3.1 mm) and thermal history. The plates of
 398 these primary alloys show similar maximum absorbed energies to the new recycled alloy. It should
 399 be noted that the new recycled alloy in T6 condition shows the best energy absorption performance
 400 compared to all primary alloy samples, a further indication that this new recycled alloy is a
 401 promising alternative for structural applications that requires energy absorption (**Figure 10**)^[34].



402
 403 **Figure 10.** Three-point bending test results of the new recycled alloy in comparison with some
 404 primary Al-Si based cast alloys (AC: as-cast). (a) force vs. displacement plot; (b) energy vs.
 405 displacement plot; and (c) maximum energy absorbed vs. maximum displacement plot.
 406

Table 4. Summary of three-point bending test results

Sample	Condition	Total Energy Absorption (J)	Max Force (kN)	Max Displacement (mm)
2 mm	AC	77 ± 17	1.4 ± 0.2	2.4 ± 0.4
	T5	66 ± 14	1.4 ± 0.2	2.2 ± 0.2
	T6	160 ± 25	1.2 ± 0.2	3.6 ± 0.2
3 mm	AC	171 ± 35	2.6 ± 0.3	2.6 ± 0.2
	T5	165 ± 24	2.7 ± 0.2	2.5 ± 0.1
	T6	478 ± 136	2.4 ± 0.2	4.3 ± 0.4
5 mm	AC	353 ± 73	5.4 ± 0.5	2.7 ± 0.4
	T5	309 ± 59	5.5 ± 0.3	2.5 ± 0.2
	T6	692 ± 185	4.8 ± 0.3	3.8 ± 0.5

408

409 The outlook for using this recycled alloy for structural automotive applications is promising
410 based on the mechanical property results obtained in this study. The most important next step is to
411 further optimize the die casting process parameters to produce more robust mechanical properties.
412 Additionally, prototype die castings will be produced for comprehensive testing of structural and
413 corrosion performance of the new alloy in automotive components.

414

415 **IV. Conclusions**

416 A new secondary aluminum alloy with a composition of Al-8.6Si-0.32Mg-0.44Fe-0.32Cu-
417 0.22Mn-0.15Zn-0.08Sr was developed for structural die casting applications. The microstructure
418 and mechanical properties of the new recycled alloy were evaluated for as-cast, T5 and T6 tempers.
419 Based on the results, the following conclusions can be drawn:

420 (1) An Fe-to-Mn ratio range of 1.65 – 3 can suppress the formation of β -Al₅FeSi phase in die
421 casting microstructure of Al-Si-Mg based cast alloys. The Fe-containing intermetallics in the as-
422 cast microstructure of the new recycled alloy included α -Al₁₅(Fe,Mn)₃Si₂ phase with polygonal

423 morphology and needle-like π -Al₈FeMg₃Si phase within interdendritic regions. Al₂Cu particles
424 were also observed formed on π -phase because of high Cu content in the new alloy.

425 (2) Both π -Al₈FeMg₃Si₂ and α -Al₁₅(Fe,Mn)₃Si₂ phases are thermodynamically stable at low
426 temperatures. Therefore, both phases were still present in the microstructure after T5 (180 °C for
427 2 hrs) treatment. In contrast, during the solution treatment (490 °C for 30 mins), π -Al₈FeMg₃Si₂
428 phase was completely dissolved into the α -Al matrix, while α -Al₁₅(Fe,Mn)₃Si₂ was partially
429 dissolved and fragmented into smaller pieces.

430 (3) The new recycled alloy has similar or slightly higher as-cast yield strength (154 MPa) but
431 slightly reduced average elongation (5.8%), compared to three major primary die cast alloys. After
432 T5 heat treatment at 180 °C for 2 hours, the yield strength is increased by 26% to 194 MPa while
433 the elongation is reduced to 3.7%. The best mechanical properties were achieved after T6 heat
434 treatment with the highest yield strength (173 MPa) and elongation (7.8%), due to the dissolution
435 of needle-like π -Al₈FeMg₃Si₂ phase and spheroidization of Si particles in the T6 microstructure.

436 (4) The relatively low elongation of the new recycled alloy, compared to primary die cast alloys,
437 was attributed to higher fractions of Fe-containing intermetallic phases, as well as porosity,
438 entrained oxides and externally solidified products found in the microstructure. The process
439 parameters of the die casting operation must be further improved to achieve the true potential of
440 the secondary alloy developed in this work.

441 (5) Excellent bendability and energy absorption of this recycled alloy was achieved, especially
442 for T6 treatment, with similar performance to primary Al-Si based structural die cast alloys. The
443 overall mechanical properties of the new recycled alloy are close to primary alloys with similar
444 composition and thermal history, which is promising for structural applications.

445

446 **Credit Authorship Contribution Statement**

447 Emre Cinkilic: conceptualization, writing, methodology, investigation; Michael Moodispaw:
448 characterization and testing, conceptualization; Jianyue Zhang: writing, sample production and
449 characterization; Jiashi Miao: characterization and testing, investigation; Alan Luo:
450 conceptualization, investigation, writing, supervision.

451 **Data Availability**

452 All data is available upon request. Please submit your request to the corresponding author.

453 **Competing Interests**

454 The authors declare no competing interest.

455 Acknowledgements

456 The authors would like to acknowledge Audubon Metals for providing secondary aluminum for
457 the die casting experiments and Dr. Xinyan Yan of Alcoa for many technical discussions. This
458 material is based upon work supported by the U.S. Department of Energy's Office of Energy
459 Efficiency and Renewable Energy (EERE) under the Advanced Manufacturing Office Award
460 Number DE-EE0007897, awarded to The REMADE Institute, a division of Sustainable
461 Manufacturing Innovation Alliance Corp. This report was prepared as an account of work
462 sponsored by an agency of the United States Government. Neither the United States Government
463 nor any agency thereof, nor any of their employees, makes any warranty, express or implied, or
464 assumes any legal liability or responsibility for the accuracy, completeness, or usefulness of any
465 information, apparatus, product, or process disclosed, or represents that its use would not infringe
466 privately owned rights. Reference herein to any specific commercial product, process, or service
467 by trade name, trademark, manufacturer, or otherwise does not necessarily constitute or imply its
468 endorsement, recommendation, or favoring by the United States Government or any agency
469 thereof. The views and opinions of authors expressed herein do not necessarily state or reflect
470 those of the United States Government or any agency thereof.

471

472 References

- 473 1 A. Taub, E. De Moor, A. Luo, D.K. Matlock, J.G. Speer, and U. Vaidya: *Annu. Rev.*
474 *Mater. Res.*, 2019, vol. 49, pp. 327–59.
- 475 2 A.A. Luo: *CIM J.*, 2021, vol. 12, pp. 79–87.
- 476 3 K. Anderson, J. Weritz, and J.G. Kaufman, eds.: *Prop. Sel. Alum. Alloy.*, 2019, 2B, vol.
477 2B.
- 478 4 G. Gaustad, E. Olivetti, and R. Kirchain: *J. Ind. Ecol.*, 2010, vol. 14, pp. 286–308.
- 479 5 G. Gaustad, E. Olivetti, and R. Kirchain: *Resour. Conserv. Recycl.*, 2012, vol. 58, pp. 79–
480 87.
- 481 6 K. Nakajima, O. Takeda, T. Miki, K. Matsubae, S. Nakamura, and T. Nagasaka: *Environ.*
482 *Sci. Technol.*, 2010, vol. 44, pp. 5594–600.
- 483 7 A.N. Løvik, R. Modaresi, and D.B. Müller: *Environ. Sci. Technol.*, 2014, vol. 48, pp.
484 4257–65.
- 485 8 S. Capuzzi and G. Timelli: *Preparation and Melting of Scrap in Aluminum Recycling: A*
486 *Review*, vol. 8, 2018.
- 487 9 D. Bösch, S. Pogatscher, M. Hummel, W. Fragner, P. Uggowitzer, M. Göken, and H.
488 Höppel: *Metall. Mater. Trans. A*, 2015, vol. 46, pp. 1035–45.
- 489 10 L. Zhang, J. Gao, L.N.W. Damoah, and D.G. Robertson: *Miner. Process. Extr. Metall.*
490 *Rev.*, 2012, vol. 33, pp. 99–157.
- 491 11 R. Lumley: *JOM*, 2019, vol. 71, pp. 382–90.
- 492 12 D. Song, Y. Zhao, Z. Wang, Y. Jia, H. Huang, D. Zhang, and W. Zhang: *J. Mater. Res.*,
493 2021, vol. 36, pp. 1357–66.
- 494 13 L.Y. Song, H.X. Liu, S.N. Nie, B.Y. Yu, S.C. Wang, L. Zheng, and R.X. Li: *Materwiss.*

- 495 *Werksttech.*, 2019, vol. 50, pp. 462–70.
- 496 14 J.A. Taylor: *Procedia Mater. Sci.*, 2012, vol. 1, pp. 19–33.
- 497 15 L. Jin, K. Liu, and X.G. Chen: *Metall. Mater. Trans. B Process Metall. Mater. Process.*
498 *Sci.*, 2019, vol. 50, pp. 1896–907.
- 499 16 J. Wang, P.D. Lee, R.W. Hamilton, M. Li, and J. Allison: *Scr. Mater.*, 2009, vol. 60, pp.
500 516–9.
- 501 17 C. Puncreobutr, A.B. Phillion, J.L. Fife, P. Rockett, A.P. Horsfield, and P.D. Lee: *Acta*
502 *Mater.*, 2014, vol. 79, pp. 292–303.
- 503 18 J.A. Taylor, G.B. Schaffer, and D.H. Stjohn: *Metall. Mater. Trans. A Phys. Metall. Mater.*
504 *Sci.*, 1999, vol. 30, pp. 1657–62.
- 505 19 C.M. Dinnis, J.A. Taylor, and A.K. Dahle: *Metall. Mater. Trans. A*, 2006, vol. 37, pp.
506 3283–91.
- 507 20 C.M. Dinnis, J.A. Taylor, and A.K. Dahle: *Scr. Mater.*, 2005, vol. 53, pp. 955–8.
- 508 21 E. Cinkilic, C.D. Ridgeway, X. Yan, and A.A. Luo: *Metall. Mater. Trans. A*, 2019, vol.
509 50, pp. 5945–56.
- 510 22 S. Ferraro, A. Fabrizi, and G. Timelli: *Mater. Chem. Phys.*, 2015, vol. 153, pp. 168–79.
- 511 23 M. Timpel, N. Wanderka, R. Schlesiger, T. Yamamoto, N. Lazarev, D. Isheim, G.
512 Schmitz, S. Matsumura, and J. Banhart: *Acta Mater.*, 2012, vol. 60, pp. 3920–8.
- 513 24 G.K. Sigworth: *Int. J. Met.*, 2008, vol. 2, pp. 19–40.
- 514 25 J.M. Yu, N. Wanderka, A. Rack, R. Daudin, E. Boller, H. Markötter, A. Manzoni, F.
515 Vogel, T. Arlt, I. Manke, and J. Banhart: *J. Alloys Compd.*, 2018, vol. 766, pp. 818–27.
- 516 26 Y.H. Cho, H.C. Lee, K.H. Oh, and A.K. Dahle: *Metall. Mater. Trans. A Phys. Metall.*
517 *Mater. Sci.*, 2008, vol. 39, pp. 2435–48.
- 518 27 S. Ji, W. Yang, F. Gao, D. Watson, and Z. Fan: *Mater. Sci. Eng. A*, 2013, vol. 564, pp.
519 130–9.
- 520 28 X. Yan, F. Caron, K. Sadyappan, and G. Birisan: in *NADCA Die Casting Congress &*
521 *Tabletop*, 2017.
- 522 29 A.A. Luo: *Calphad-Computer Coupling Phase Diagrams Thermochem.*, 2015, vol. 50, pp.
523 6–22.
- 524 30 M.A. Moustafa, F.H. Samuel, and H.W. Doty: *J. Mater. Sci.*, 2003, vol. 8, pp. 4507–22.
- 525 31 A. Gorny, J. Manickaraj, Z. Cai, and S. Shankar: *J. Alloys Compd.*, 2013, vol. 577, pp.
526 103–24.
- 527 32 Y. Du, Y.A. Chang, B. Huang, W. Gong, Z. Jin, H. Xu, Z. Yuan, Y. Liu, Y. He, and F.Y.
528 Xie: *Mater. Sci. Eng. A*, 2003, vol. 363, pp. 140–51.
- 529 33 M.Y.A. Youssef: *A cost-efficient process route for the mass production of thin-walled*
530 *structural aluminum body castings*, Doctoral Dissertation, RWTH Aachen University,
531 2021, pp. 107-111.